

Using Surface Remote Sensors to Derive Radiative Characteristics of Mixed-Phase Clouds: An Example from M-PACE

Gijs de Boer^{1,2}, William D. Collins¹, Surabi Menon¹, and Charles N. Long³

¹Lawrence Berkeley National Laboratory, Berkeley, CA, USA

²Cooperative Institute for Research of Environmental Sciences, Boulder, CO, USA

³Pacific Northwest National Laboratory, Richland, WA, USA

Correspondence to: Gijs de Boer
(GDeBoer@lbl.gov)

Abstract. Measurements from ground-based cloud radar, high spectral resolution lidar and microwave radiometer are used in conjunction with a column version of the Rapid Radiative Transfer Model (RRTMG) and radiosonde measurements to derive the surface radiative properties under mixed-phase cloud conditions. These clouds were observed during the United States Department of Energy (US DOE) Atmospheric Radiation Measurement (ARM) Mixed-Phase Arctic Clouds Experiment (M-PACE) between September and November of 2004. In total, sixteen half hour time periods are reviewed due to their coincidence with radiosonde launches. Cloud liquid (ice) water paths are found to range between 11.0-366.4 (0.5-114.1) gm^{-2} , and cloud physical thicknesses fall between 286-2075 m. Combined with temperature and hydrometeor size estimates, this information is used to calculate surface radiative flux densities using RRTMG, which are demonstrated to generally agree with measured flux densities from surface-based radiometric instrumentation. Errors in longwave flux density estimates are found to be largest for thin clouds, while shortwave flux density errors are generally largest for thicker clouds. A sensitivity study is performed to understand the impact of retrieval assumptions and uncertainties on derived surface radiation estimates. Cloud radiative forcing is calculated for all profiles, illustrating longwave dominance during this time of year, with net cloud forcing generally between 50 and 90 Wm^{-2} .

1 Introduction

The radiative impacts of clouds remain one of the largest uncertainties in the simulation and understanding of global climate change (IPCC, 2007). In particular, clouds occurring in the Arctic have a potentially large impact on characteristics and lifetime of sea ice (e.g. Kay and Gettelman, 2009),

permafrost, and plant growth (e.g. Prowse et al., 2009). Of clouds observed at high latitudes, mixed-phase stratiform clouds, containing both ice and liquid hydrometeors, are among the most-commonly observed, longest lasting and radiatively influential cloud structures (e.g. Curry et al., 1996; Shupe et al., 2006). As discussed in Shupe et al. (2008a), observation of these clouds is inherently difficult
25 due to the need to capture multiple phases of water simultaneously.

Despite these challenges, several previous efforts have provided estimates of Arctic stratiform cloud radiative characteristics and forcing. While obtaining this estimate is not the central goal of the present study, we do provide an overview of these studies and their methodologies for reference. Pioneering estimates of infrared radiative characteristics of summertime stratiform clouds
30 over the Beaufort Sea were provided by Curry and Herman (1985) using a combination of radiometers, in-situ measurements and a radiative transfer model. In that work, cloud emittances, absorption coefficients, reflectances, cooling rates and extinction lengths were reported. All parameters were found to be strongly tied to liquid cloud droplet size distributions assumed and cloud liquid water path (LWP). Expanding on this work, Curry and Ebert (1992) utilized measurement-based estimates
35 of cloud fraction and microphysical properties, along with top of the atmosphere (TOA) radiative flux densities from the NASA Earth Radiation Budget Experiment (ERBE; Barkstrom et al., 1990) to calculate an annual cycle of radiative flux densities for different cloud types. Included in their analysis were “low clouds”, parameterized to have mean seasonal LWP between 10-40 gm^{-2} and ice water paths between 0-60 gm^{-2} . The uncertainty associated with estimating cloud droplet ef-
40 fective radius was mentioned to be considerable. Net surface cloud forcing was demonstrated to be positive throughout most of the year, with any negative values occurring during the summer months, when cloud-induced shortwave cooling is slightly stronger than longwave heating.

Utilizing a combination of surface-based and in-situ measurements from the Beaufort and Arctic Storms Experiment (BASE), National Centers for Environmental Prediction (NCEP) modeled syn-
45 optic scale properties and a two-stream radiative transfer model, Pinto (1998) demonstrated good agreement between measured longwave radiative flux densities and those observed. Comparison of model calculations with clear-sky calculations demonstrated a longwave cloud radiative forcing of up to 70 Wm^{-2} . Shupe and Intrieri (2004) provide cloud radiative forcing calculations for an annual cycle of clouds observed during the Surface Heat Budget of the Arctic (SHEBA; Uttal et al., 2002),
50 analyzing individual contributions of cloud properties on long and shortwave forcing for observed clouds. They found that clouds with significant longwave impacts were generally low clouds with warmer base temperatures, with longwave cloud forcing impacted strongly by LWP. Except during mid-summer, they found that longwave effects dominate up to LWP values of 400 gm^{-2} . They also demonstrated that for clouds containing liquid water, the longwave forcing dominates net cloud
55 forcing on an annual scale, resulting in a peak in the annual distribution of net cloud radiative forcing of approximately 50 Wm^{-2} . The largest net cloud radiative forcing was demonstrated to occur during fall, when liquid clouds are thickest and solar radiation is reduced. An annual distribution of

longwave cloud forcing for liquid-containing clouds was found to peak at 50-70 Wm^{-2} . Summer cloud radiative forcing was also evaluated by Dong and Mace (2003). Utilizing surface remote sensors at Barrow for May-September, they found the net radiative forcing by stratus clouds to become negative starting in late May, and stay negative until early September. The forcing was found to peak during June and July, with values up to -150 Wm^{-2} . Stratus cloud longwave radiative forcing was found to range between roughly 40-70 Wm^{-2} during that time period.

In the current effort, we utilize modern measurement and retrieval methods from a combination of ground-based remote sensors used during the Mixed-Phase Arctic Cloud Experiment (M-PACE; Verlinde et al., 2007) to derive surface radiative characteristics under mixed-phase cloud conditions observed during this campaign. Instruments included are the DOE Millimeter Cloud Radar (MMCR), the University of Wisconsin High Spectral Resolution Lidar (AHSRL) and a microwave radiometer (MWR). While surface radiative measurements are available for this time period, our main focus is characterizing the ability of a combination of remotely-sensor measurements and a column version of the advanced Rapid Radiative Transfer Model (RRTMG; Clough et al., 2005) to derive the surface radiative flux densities. We quantify the sensitivity of this technique to retrieval assumptions, and put it forward as a substitute for traditional radiometric measurements in situations where radiometric measurements are lacking or limited. Use of remotely-sensed measurements for calculating radiative properties provides more information about the vertical structure of the clouds than surface radiation measurements alone, and can be useful in the evaluation of new retrieval methods through radiative closure studies. To provide a thorough characterization, we additionally perform experiments analyzing this method's sensitivity to less frequently measured quantities such as surface temperature and surface albedo. An overview of methods and tools utilized is provided in the following section. This is followed by an overview of M-PACE clouds studied, an analysis of derived surface flux density estimates, a sensitivity analysis and cloud radiative forcing calculations. Finally a summary is provided.

2 Measurement Period and Methods

M-PACE was a United States Department of Energy (DOE) Atmospheric Radiation Measurement (ARM) experiment carried out along the north slope of Alaska (NSA) during autumn of 2004 aimed at collecting a focused set of observations to better understand Arctic mixed-phase clouds. Measurements used in this evaluation were collected at Barrow (71.3°N, 156.6°W). The current approach requires observations taken close to a radiosonde sampling time (00Z and 12Z). With this restriction 16 cases featuring single-layer mixed-phase stratiform clouds were identified, covering a wide variety of cloud thicknesses, as well as liquid and ice water paths for both day and nighttime periods (see Table 1).

2.1 Instruments and Retrievals

To derive cloud properties, we utilized a combination of ground based remote sensors and information from launched radiosondes. The microphysical retrieval techniques implemented are similar to those described in de Boer et al. (2009) and Shupe et al. (2008b), using the University of Wisconsin Arctic High Spectral Resolution Lidar (AHSRL; Eloranta, 2005), a 35-GHz Millimeter Cloud Radar (MMCR; Moran et al., 1998) and microwave radiometer (MWR). Our focus on mixed-phase stratiform clouds is due in part to the challenge they present to microphysical retrieval algorithms. Retrievals implemented generally represent state-of-the-science attempts, as recommended by Shupe et al. (2008a), and outlined here.

To begin, cloud boundaries are determined using the cloud radar and lidar. A combination of AHSRL backscatter cross-section and depolarization is used to find the base of the liquid component of the cloud (Z_{base}). All ice found below that is assumed to be precipitation. Because the lidar signal is often completely attenuated within the cloud layer, MMCR reflectivity is used to find cloud top (Z_{top}). It is important to note that due to near-field limitations of the radar, observations below 200m are not included in any of the analysis presented. Cloud base and top temperatures for each profile are derived using this information in combination with radiosonde temperature measurements.

Ice water content (IWC) is calculated using an empirical relationship from radar reflectivity (Z_{mmcr}) as prescribed in Shupe et al. (2006). The relationship used is:

$$IWC = 0.07Z_{mmcr}^{0.63} \quad (1)$$

While this equation is empirical, and tuned to measurements taken during the Surface Heat Budget of the Arctic Ocean campaign (SHEBA, Uttal et al., 2002), it is generally the best option available, since multi-sensor retrievals are limited by attenuation of the lidar and a liquid-dominated lidar backscatter signal. While a similar relationship was derived specifically for M-PACE in Shupe et al. (2008b), with the only change being an updated leading coefficient (0.04 instead of 0.07), the SHEBA relationship is believed to be more universally applicable and is therefore used here. The sensitivity of radiative estimates to this relationship is explored in Section 3.3.

Because the liquid cloud can not necessarily be detected by the radar, and attenuation hinders lidar measurements, liquid water content (LWC) is calculated using a scaled-adiabatic assumption (Zuidema et al., 2005). Utilizing radiosonde temperature information, the pseudo-adiabatic lapse rate (Γ_s) for a cloud is calculated. From this, we calculate liquid water mixing ratio (w_l) via integration of:

$$dw_l = \frac{c_p}{L_{l,v}} \left(\Gamma_s + \frac{g}{c_p} \right) dz \quad (2)$$

with c_p being the specific heat of air at a constant pressure, $L_{l,v}$ the latent heat of vaporization, z the altitude, and g the acceleration due to gravity. Multiplication of the liquid water mixing ratio by the air density results in an estimate of LWC. Since these clouds are not necessarily adiabatic, we scale

the calculated profile using LWP derived from MWR measurements. Because this method depends on accurate temperature measurements, we can only calculate these properties close to radiosonde launches, and have limited our analysis here to +/- 15 minutes from the radiosonde analysis time.

130 Ice and liquid hydrometeor effective sizes are more challenging to derive. For ice effective particle size ($r_{e,ice}$), we utilize a multi-instrument retrieval (AHSRL and MMCR) as described in Donovan and van Lammeren (2001), using the ratio of lidar and radar backscatter to estimate particle effective size. This technique requires an assumed ice crystal habit governing the power law relationship used to relate ice crystal size and volume (e.g. Mitchell, 1996). This size retrieval can only be done below
135 the liquid portion of the cloud due to dominance of the lidar signal by the liquid component of the mixed-phase cloud. Therefore, once inside the cloud layer, we utilize a scaling factor calculated just below cloud base based on the ratio of radar reflectivity just below cloud base to radar reflectivity throughout the cloud. This ratio is raised to the 1/6th power, since radar backscatter cross section is proportional to r^6 . Values of $r_{e,ice}$ within the cloud layer are then calculated using this scaling factor
140 and the below cloud $r_{e,ice}$. Liquid droplet effective radius ($r_{e,liq}$) is not constrained, since we can not observe the depth of the liquid component of the cloud. Therefore, calculate a profile of $r_{e,liq}$ that assumes an initial cloud-base droplet size, and scales to the LWC profile, assuming a constant droplet number concentration calculated using this cloud-base droplet size and LWC.

An example of the measurements and retrievals is provided in Figure 1. Included in the top
145 half of Figure 1 are plots of AHSRL-measured backscatter cross-section (β' ,top) and depolarization (δ ,middle), as well as MMCR reflectivity (Z_{mmcr} ,bottom). The data have been averaged to 2-minute intervals in order to reduce noise and variability in the information passed into the radiative transfer model. Higher values of β' observed at roughly 500-800m are the result of liquid droplets. Because of the concentration of these droplets, they have a large combined backscatter cross-section. AHSRL
150 δ is used to help determine cloud phase, with lower depolarization ratios generally resulting from spherical scatterers. Due to the thickness of the liquid portion of this cloud, the lidar signal is attenuated before reaching cloud top. This is seen in Z_{mmcr} , which demonstrates detected hydrometeors up to roughly 1300 m. Because of the longer wavelength utilized, the MMCR is more sensitive to ice crystals, and likely can not detect cloud-top liquid droplets. However, in-situ and remote-sensing
155 studies have demonstrated that ice crystals generally extend up to cloud top (e.g. de Boer et al., 2008; McFarquhar et al., 2007), and that radar is capable of detecting cloud top altitude.

The lower half of Figure 1 illustrates profiles of retrieved liquid and ice water content, as well as liquid and ice particle sizes for the 10 October case. These provide some perspective on the variability between individual profiles within a case. Because of the pseudo-adiabatic assumption
160 applied to the liquid portion of the cloud, liquid properties vary relatively linearly with altitude. Ice properties demonstrate more variability with altitude.

2.1.1 RRTMG

RRTMG is a global climate model version of the rapid radiative transfer model (RRTM). It calculates long and shortwave flux densities utilizing a correlated-k method for computational efficiency.

165 It has been demonstrated to be accurate when compared to line-by-line radiative calculations. Parts of RRTM are currently implemented in the European Center for Medium-Range Weather Forecasts (ECMWF) and National Centers for Environmental Prediction (NCEP) Global Forecast System (GFS) models, as well as the latest version of the National Center for Atmospheric Research (NCAR) Community Climate System Model (CCSM4) as part of the Community Atmosphere Model (CAM).
170 In this work, retrieved profiles of LWC, IWC, $r_{e,ice}$, and $r_{e,liq}$, solar zenith angle, surface temperature and albedo are used to drive a column version of RRTMG. Solar zenith angle is calculated for each given date and time, along with the earth's radius at Barrow's latitude. One drawback of using RRTMG in this evaluation is that the model assumes a plane-parallel atmosphere. Because of the high sun-angles involved, the attenuation of the solar beam is likely overestimated because of
175 an increase in the atmospheric path length resulting from the plane-parallel assumption. Finally, assigned profiles of carbon dioxide, ozone, nitrous oxide, carbon monoxide and methane included with the RRTM package are based on a sub-Arctic atmosphere. A profile of water vapor is determined directly from the radiosonde measurements.

3 Analysis

180 3.1 Derived Cloud Properties

Although only a small sample, clouds observed close to radiosonde launches during M-PACE cover a variety of mixed-phase stratiform conditions. Estimates of mean cloud thickness (ΔZ_{liquid}), mean cloud LWP and mean cloud ice water path (IWP) are provided in Table 1 for each of the 16 cases analyzed. Figure 2 provides additional insight into variability between and within cases. For each
185 quantity, boxplots are laid out with the black line representing the mean, shaded boxes representing the interquartile range (IQR) and whiskers representing 1.5xIQR beyond the 25th and 75th percentiles (roughly 2.7σ for normally distributed datasets) for measured profiles within each case. Points outside of this range are represented by open circles. It is important to note that 2-minute averaging results in only 6 to 15 profiles per case (depending on instrument calibrations and uptime),
190 meaning small sample sizes for the distributions shown. Cloud base temperature for these cases was found to vary between 253-272 K. Due to the stratiform nature of the clouds, temperature generally did not vary very much within each case. Cases 11-16, occurring later in the year (end of October, beginning of November) had the coldest recorded temperatures.

Liquid cloud thickness varied between 300 and 1600 m, and within case 2, varied up to 400 m.
195 Generally, clouds were found to be around 800 m thick. Retrieved LWP also varied substantially

between cases, ranging from roughly 10 gm^{-2} to over 350 gm^{-2} . With the exception of cases 12 and 15, these clouds contained enough liquid (in a mean sense) to emit as grey bodies. The LWP threshold for this was demonstrated to be around 30 gm^{-2} by Shupe and Intrieri (2004), with further increases in LWP having no impact on downwelling longwave radiation.

200 As discussed above, liquid droplet effective radii were constrained by measured LWP, via the scaled liquid water content. In Figure 2, all cases were assumed to have cloud droplet effective radii of $3.5 \mu\text{m}$ at cloud base, and grow larger with height. Therefore, it is not surprising that mean cloud droplet effective radius ($\bar{r}_{e,liq}$) appears to scale with cloud physical depth. Using this initial value, $\bar{r}_{e,liq}$ ranged from roughly $4\text{-}5.8 \mu\text{m}$.

205 Ice water paths were found to vary quite widely, both between cases and within individual cases. Across the dataset, values varied between roughly $0.5\text{-}200 \text{ gm}^{-2}$, though with the exception of case 14, case mean values did not exceed 135 gm^{-2} . Mean ice particle effective radii ($\bar{r}_{e,ice}$) were estimated to fall between $15\text{-}80 \mu\text{m}$. Generally, variability for any individual case was small (with exception of case number 4), and $\bar{r}_{e,ice}$ generally fell between 30 and $50 \mu\text{m}$.

210 3.2 RRTMG Derived Flux Densities

Initial analysis is completed on all 16 cases, assuming cloud-base $r_{e,liq}$ of $3.5 \mu\text{m}$, bullet rosettes as the ice crystal habit, and using retrieved cloud properties. Surface albedos for each case were calculated from surface radiometric data, with case-mean values ranging between 0.67 and 0.86 . Finally, ground temperature was obtained from the National Oceanographic and Atmospheric Administration's (NOAA) US Climate Reference Network station at Barrow, which uses a Apogee Instruments IRTS-P infrared (IR) temperature sensor mounted on a tower at 1.3 meters above ground level. An evaluation of RRTMG-derived flux densities is completed using QC RAD, a quality-controlled surface radiation estimate product available through the ARM program database (Long and Shi, 2008). Results of this evaluation are shown in Figure 3. Shortwave (wavenumbers between 820 and 215 50000 cm^{-1}) and longwave (wavenumbers between 10 and 3250 cm^{-1}) flux densities are shown, and broken down into surface downwelling, upwelling and net components. Each case features two distributions, with boxplots plotted identically to Figure 2. Outlying values (values outside of the IQR ± 1.5 IQR) are shown by open circles. The sign convention used results in positive net values at the surface when downwelling flux density is larger than upwelling flux.

225 Generally speaking, intra-case variability is found to be greatest for surface shortwave radiation, with net surface shortwave flux densities changing by as much as 20 Wm^{-2} . General patterns observed were replicated in the modeled data. The best agreement was found for downwelling longwave radiation, with a root-mean-squared error (RMSE) of 4.48 Wm^{-2} . The upwelling longwave estimates had larger errors (RMSE of 9.18 Wm^{-2}), likely due to errors in the surface temperature 230 estimates used. Combined, these result in RMSE of 9.83 in the net surface longwave flux densities. For all of these quantities, it should be noted that the majority of the error seems to come from a

small subset of the cases, with cases 11, 13 and 14 having the largest differences between modeled and observed surface flux densities. As is shown in Figure 2, these cases feature some of the smallest LWP observed. Shortwave errors were generally larger. RMSEs for downwelling, upwelling and net shortwave radiation were 9.93, 7.27 and 2.78 Wm^{-2} respectively. These numbers are muted due to contributions from nighttime cases, where both modeled and observed flux densities were zero. Removing nighttime cases, these values were increased to 14.43, 10.57 and 4.04 Wm^{-2} . Some of this error is likely due to the assumption of a plane-parallel atmosphere employed in RRTMG.

Error magnitude was also plotted against visible optical depth for each case (Fig. 4). The optical depths were computed separately for the liquid and ice components using relationships from Stephens (1994) and Ebert and Curry (1992), respectively. The relationship for liquid is:

$$\tau_{vis,liq} \approx \frac{3LWP}{2\rho_l r_{e,liq}} \quad (3)$$

where $\tau_{vis,liq}$ is the visible optical depth for liquid, LWP is the liquid water path, ρ_l is the density of water, and $r_{e,liq}$ is the droplet effective radius. For ice, the relationship is:

$$\tau_{vis,ice} \approx IWP \left[a + \frac{b}{r_{e,ice}} \right] \quad (4)$$

where $\tau_{vis,ice}$ is the visible optical depth for ice, IWP is the ice water path, $r_{e,ice}$ is the ice crystal effective size, and a and b are wavelength-dependent parameters (available in Ebert and Curry (1992), for visible wavelengths $a=3.448 \times 10^{-3} \text{ m}^2 \text{ g}^{-1}$ and $b=2.431 \mu\text{m m}^2 \text{ g}^{-1}$).

For shortwave flux densities illustrated in Figure 4, it appears that errors in both up- and downwelling flux densities increase with increasing τ_{vis} for both liquid and ice. Generally, shortwave flux densities appear to be underestimated by the technique used. The cluster of cases that demonstrate zero error are the result of dark or very low-light cases, with nighttime cases (solar zenith angle $\geq 90^\circ$) illustrated in red. Errors in up- and downwelling components look very similar to one another due to the upwelling component simply being proportional to the downwelling by the albedo. It also appears as though clouds with lower LWP provide more difficulties for the model than thicker clouds, and that clouds with low $\tau_{vis,ice}$ are the only ones that over predict incoming (and therefore outgoing) shortwave radiation. Net shortwave flux density errors are generally less than 10 Wm^{-2} .

For longwave flux densities, again the errors in net surface radiative flux density are relatively small (generally $< 10 \text{ Wm}^{-2}$). Downwelling longwave flux densities seem to be over-predicted, with errors $< 3 \text{ Wm}^{-2}$ for cases with larger $\tau_{vis,liq}$. Cases with smaller $\tau_{vis,liq}$ have errors up to roughly 10 Wm^{-2} . The center column of Figure 4 illustrates boxplots (similarly laid out to Figure 2) illustrating the distribution of errors for each flux density component. For shortwave flux densities, nighttime errors were not included in these boxplots. Mean error values are presented in Table 2.

3.3 Sensitivity Analysis

In order to assess the sensitivity of these estimates to retrieval error and missing measurements, 56 sensitivity experiments were completed. Retrievals were re-calculated modifying a series of

different quantities, including the ice crystal habit assumed, the liquid droplet effective size at cloud base, the MWR-retrieved LWP, and the radar derived IWC. The ice crystal habit was varied between bullet rosettes, spheres and broad-branched crystals, changing the coefficients for the power-law relationships used to retrieve the ice crystal effective size. Liquid droplet effective size was tested at both 3.5 μm (lower limit acceptable for RRTMG), and 6.5 μm . Since this droplet size is what is assumed at cloud base, it should be indicative of a newly nucleated droplet. With some assumptions about aerosol composition, a 3.5 μm droplet would nucleate on an aerosol particle of 0.2 (0.4) μm at 0.1 (1.0) % supersaturation with respect to water. The 6.5 μm size was chosen as a realistic upper limit, with droplets of that size forming on aerosol particles with radii of 0.4 (1.0) μm at 0.1 (1.0) % supersaturation with respect to water (de Boer et al., 2010). In changing droplet size, LWP was always held to the measured value, resulting in variable liquid optical depths. While not presented here, the range covered by these optical depths can be calculated using Equation 3. LWP values were varied by $\pm 25 \text{ gm}^{-2}$, the derived uncertainty for this method (Westwater et al., 2001). The sensitivity to retrieved IWC was evaluated in two ways. First, IWC derived by the MMCR was varied by $\pm 75\%$, the uncertainty derived for this method by Shupe et al. (2006). Second, sensitivity to the leading coefficient used in the empirical Z-IWC relationship was evaluated. This was done based on the use of 0.04 as a leading coefficient for M-PACE clouds in Shupe et al. (2008b). Finally, an overall analysis of all possible combinations of these perturbations was performed to derive net retrieval sensitivity. Please note that the impact of the leading coefficient in the IWC retrieval was not included in this net analysis. The quantity used to illustrate the sensitivity is the difference in derived flux densities under perturbed conditions from those derived assuming the base conditions described at the start of Section 3.2.

Results from this evaluation are shown in Figure 5 for downwelling long- (blue) and shortwave (red) flux densities. Since upwelling longwave flux density is simply a function of surface temperature and upwelling shortwave flux density is a function of surface albedo, differences in these values are not evaluated here. As with other box plots, the mean value is shown by the black line, the IQR is represented by the box, and 1.5xIQR beyond the 25th and 75th percentiles is represented by the whiskers. For this figure, outliers are not shown. In general, uncertainties in liquid property retrievals impact estimates more strongly than those associated with ice. With the exception of sensitivity associated with the liquid droplet effective radius, variability is generally less than 15 Wm^{-2} for individual parameters, based on the IQR ± 1.5 xIQR derived from all profiles.

Changes in assumed ice crystal habit appear to impact shortwave flux density estimates at a level comparable to changes in cloud LWP. However, while uncertainty of LWP estimates is well quantified, no such information is available for ice crystal shape in these mixed-phase stratiform clouds. Despite this, it is unlikely that either spherical ice or broad-branched crystals are truly representative of the distribution of ice crystal shapes found, resulting in an extreme estimate of sensitivity. Liquid droplet size has a larger impact, particularly on shortwave flux densities. In addition to these

shortwave sensitivities, there are also some minimal impacts on longwave downwelling radiation.

305 For the thinnest cases sampled, cloud impact on downwelling longwave radiation is not as dominant as for thicker clouds. In these instances, increasing $r_{e,liq}$ decreases cloud optical depth, resulting in an increased contribution to downwelling surface longwave flux density from the clear sky above cloud level, reducing the effective atmospheric radiating temperature. This results in decreased flux density at the surface with increasing $r_{e,liq}$. Changing LWP impacts shortwave flux densities through

310 changes in cloud optical depth, while also altering the surface downwelling longwave flux density. IWC has the smallest impact on the surface flux densities. Sensitivity to the leading coefficients (IWC_C) previously presented in the literature for Z-IWC relationships (0.04 and 0.07) has minimal impact on the surface radiation. A more thorough retrieval uncertainty number of 75% (IWC_U) causes slightly larger deviations, but even those are small compared to those resulting from liquid

315 water property uncertainties. To evaluate the relative importance of ice properties, all cases were run with ice influences removed. The result of this comparison is shown on the far right of Figure 5, with ice removal resulting in increased downwelling shortwave radiation of 0-5 Wm^{-2} , and decreased downwelling longwave radiation of 0-8 Wm^{-2} . These changes are generally small when compared to the absolute magnitude of flux density, meaning that the ice contribution to the radiative

320 profile is generally a small one. Evaluating the impact of all possible combinations of the four leftmost parameters presented (i.e. not including IWC_C) results in uncertainties of roughly 10 Wm^{-2} (IQR) in the shortwave flux density and 4 Wm^{-2} (IQR) in the longwave.

While outside of the cloud property retrievals, surface characteristics also impact the surface radiation budget. As would be expected, surface shortwave flux densities demonstrate significant

325 sensitivity to the assumed surface albedo. Changes in downwelling shortwave flux density of up to 80 Wm^{-2} and up to 100 Wm^{-2} in the upwelling surface shortwave radiative flux density result from changes in the surface albedo between 95% and 50%. The largest changes occur at the upper end of this scale, with changes from 95% to 90%, for example, resulting in larger decreases in surface shortwave flux density than changes from 60% to 55%. Throughout M-PACE, as solar zenith angle

330 decreases, sensitivity to surface albedo is reduced substantially. This is also evident when comparing the sensitivities from this study to those from Shupe and Intrieri (2004), who demonstrated a decreased surface flux density of roughly 40 Wm^{-2} for every 0.1 decrease in surface albedo for conditions featuring a 60° SZA, 0.6 surface albedo and 50 gm^{-2} LWP. For case one conditions (SZA of 75°, 0.6 surface albedo and 150 gm^{-2} LWP) that sensitivity is closer to 5 Wm^{-2} per 0.1

335 decrease in surface albedo due to the lower SZA and thicker cloud. In addition to the impact of surface albedo on shortwave flux densities, surface temperature impacts upwelling surface longwave radiation. For the cases from M-PACE, a five degree decrease in surface temperature resulted in a decrease in upwelling longwave surface flux density of roughly 20 Wm^{-2} .

3.4 Derived Cloud Radiative Forcing

340 As an example of a tangible end-product derived from the calculated flux densities, cloud radiative forcing may be derived in a method similar to that used in Ramanathan et al. (1989). Here the short and longwave radiative forcing are defined as:

$$CF_{LW} = LW_{NET}(cloudy) - LW_{NET}(clear) \quad (5)$$

$$CF_{SW} = SW_{NET}(cloudy) - SW_{NET}(clear) \quad (6)$$

345 $CF = CF_{LW} + CF_{SW} \quad (7)$

where LW_{NET} and SW_{NET} the net surface long- and shortwave flux densities, respectively, and "cloudy" and "clear" terms represent the cloudy and clear-sky flux density, respectively. As in the rest of the paper, all flux densities are defined as positive downward. In order to determine the clear sky flux density, RRTMG was run on each case after removal of liquid and ice and adjustment of the temperature profile to remove inversions caused by cloud-top cooling. Inversions were removed via
350 linear interpolation of temperature from the surface to the top of the cloud-induced inversion.

Cloud radiative forcing estimates from this calculation are presented in Figure 6. Distributions of shortwave, longwave, and net cloud radiative forcing are provided for the 151 retrieved profiles. The contribution of nighttime and low light cases is evident in the large peak in shortwave forcing
355 centered on 0 Wm^{-2} . The rest of the cases are distributed on the negative side between 0 and -50 Wm^{-2} (cloud results in reduced shortwave surface flux) due to variability in cloud properties and solar zenith angle. Longwave radiative forcing is positive, with a large peak around $75\text{-}85 \text{ Wm}^{-2}$. Both longwave and shortwave distributions are qualitatively similar to those collected by Shupe and Intrieri (2004) for a year of measurements from the SHEBA campaign. However, longwave
360 cloud radiative forcing values are slightly higher ($70\text{-}90 \text{ Wm}^{-2}$ compared to $25\text{-}75 \text{ Wm}^{-2}$) when compared to the Shupe and Intrieri (2004) study. This is likely due to the short time period covered in the current study, and the likely inclusion of numerous thin liquid clouds in the one-year SHEBA dataset. The longwave values are higher but comparable to those reported by Dong and Mace (2003) for summer months in Barrow ($40\text{-}70 \text{ Wm}^{-2}$). Short- and longwave cloud radiative
365 forcing estimates for Barrow during October from Dong et al. (2010) were smaller in magnitude than those derived in the current study, but their analysis was not limited to mixed-phase clouds or liquid-containing clouds. Combined, the short- and longwave contributions result in a positive cloud radiative forcing for mixed-phase stratiform clouds observed during the M-PACE campaign. Net values range between roughly 25 and 90 Wm^{-2} , with a majority of cases falling in the $70\text{-}90 \text{ Wm}^{-2}$
370 range. This means that mixed-phase clouds increase incoming radiation at the surface due to the longwave contributions during the observed autumn period. An overview of mean cloud radiative forcing estimates is provided in Table 3.

Figure 7 demonstrates the sensitivity of cloud radiative forcing to several relevant properties. In the top row, shortwave cloud forcing is normalized to remove variation due to solar zenith angle (SZA). Here, normalized cloud forcing is defined as:

$$CF_{SW,NORM} = \frac{SW_{NET}(clear) - SW_{NET}(cloudy)}{SW_{NET}(clear)} \quad (8)$$

where $SW_{NET}(cloudy)$ is the calculated net cloud flux in the presence of clouds, and $SW_{NET}(clear)$ is the value calculated under clear sky conditions, as described above. The remaining rows show calculated cloud radiative forcing as described in equations 5-7. Nighttime cases are not included in this top row, since the denominator of Equation 8 would be zero.

On the far left, normalized shortwave, absolute shortwave, longwave and net radiative forcing are shown as a function of SZA as observed during M-PACE. As expected, absolute shortwave cloud radiative forcing becomes more negative with decreasing SZA (decreasing SZA means that the sun is higher in the sky). Cases for which the SZA was 90 are indicative of a sun that is at or below the horizon, and all calculated SZA values higher than 90 were set to 90 degrees. While longwave forcing is shown to decrease with increasing SZA, this is likely due to decreases in temperature at later times of year. The second column from the left demonstrates the relationship between liquid optical depth and cloud radiative forcing. The most noticeable influence is on the longwave cloud forcing, with a sharp decrease in cloud forcing associated with very low optical depths. This is due to a cold overlying atmosphere combined with increased cloud transmissivity in cases with low optical depths. A similar effect can be seen with the ice water optical depth (center column), though it is not nearly as well-defined.

The effect of cloud base temperature is shown in the second column from the right. As expected, lower cloud base temperatures result in decreased longwave cloud radiative forcing at the surface. In the cases presented, it appears as though clouds with the lowest liquid water optical depth also featured the lowest cloud base temperatures. For non-nighttime cases, shortwave cloud radiative forcing also increases in magnitude (becomes more negative) with increasing cloud base temperature. This relationship holds in the normalized analysis, indicating that this is not simply a result of colder clouds occurring at times with low sun angles. In support of this, thinner clouds were found to occur at colder temperatures, independent of SZA. Longwave cloud radiative forcing demonstrates a relationship to cloud thickness similar to that of the liquid optical thickness. Clouds over approximately 600 m thick had similar longwave cloud radiative forcing of 75 Wm^{-2} or larger. As with cloud base temperature, normalized shortwave cloud radiative forcing demonstrates a clear relationship to cloud thickness. This relationship is masked by SZA contributions in the raw forcing calculation.

4 Summary

Surface radiative properties were estimated for mixed-phase cloud conditions observed during M-PACE using a combination of modern cloud remote-sensors, current cloud measurements and re-

trievals and an advanced radiative transfer model. Using profiles of cloud properties such as liquid and ice water paths, cloud heights, effective particle sizes and temperature profiles to drive the radiative transfer model, a total of 16 mixed-phase cloud cases were evaluated. This technique was demonstrated to generally agree well with surface radiometric estimates, with the magnitude of most errors falling below 10 Wm^{-2} . For shortwave radiation, errors were found to be largest for clouds with thicker liquid components, and were generally found to be negative, meaning the model flux densities were too low when compared to the observations. Errors in downwelling longwave radiation were largest for clouds with low LWP, and generally positive, meaning the model flux densities were too high compared to those observed.

The calculated flux densities were used to calculate cloud radiative forcing for these mixed-phase clouds. Shortwave forcing was generally small, due in part to the contribution of nighttime cases, and in part to low sun-angles during this time of year. The largest shortwave forcing occurred early in the observation period and was roughly -50 Wm^{-2} . Longwave cloud forcing was always positive, with most values falling between $70\text{-}90 \text{ Wm}^{-2}$. Combined with the shortwave forcing, this resulted in net cloud forcing ranging between $25\text{-}90 \text{ Wm}^{-2}$. This demonstrates that these clouds act to warm the surface during the fall, which agrees with findings presented in several other studies (e.g. Schweiger and Key, 1994; Intrieri et al., 2002; Shupe and Intrieri, 2004). Shortwave cloud forcing was demonstrated to correlate strongly with solar zenith angle, with an average change of 3 Wm^{-2} per degree. Shortwave cloud forcing also appears to be correlated with cloud-base temperature, although it is likely that this is a result of colder clouds occurring during times with lower solar zenith angles. Longwave cloud forcing was shown to be connected to both liquid optical depth and physical cloud thickness. The relationship to liquid optical depth reaches an asymptote of roughly 85 Wm^{-2} for optical depths greater than 30 or so, while the relationship to cloud thickness reaches the same level for clouds thicker than 800 m.

The information presented here is relevant to understanding the impact of clouds on a changing surface state. The radiative impacts of specific cloud types on the freezing and melting of sea ice, permafrost and glaciers, for example are just beginning to be explored. Results presented provide guidance on use of this technique for expanding our knowledge of mixed-phase cloud forcing at observational sites that have cloud remote sensors but lack or have limited radiometric instrumentation. Future work will focus on application of this method to larger datasets, and exploration of the radiative impact of mixed-phase stratiform clouds on surface ice melting rates. Doing so will provide information on the relevance of clouds and cloud-aerosol effects on the climate system, as well as help us to understand how simulated future changes in cloud types and cloud cover may impact the surface state.

Acknowledgements. LBNL research was supported by the Director, Office of Science, Office of Biological and Environmental Research of the U.S. Department of Energy under Contract No. DE-AC02-05CH11231 as part of their Climate and Earth System Modeling Program. Dr. Long is supported by the Office of Biological and

445 Environmental Research (OBER) of the U.S. Department of Energy (DOE) as part of the Atmospheric Radiation
Measurement (ARM), and Atmospheric Systems Research (ASR) Programs. The Pacific Northwest National
Laboratory (PNNL) is operated by Battelle for the DOE under contract DE-AC06-76RLO 1830. LBNL is
managed by the University of California under U.S. DOE grant DE-AC02-05CH11231. The authors would
like to thank Michael Iacono and the Atmospheric and Environmental Research (AER) team for their help in
450 setting up RRTMG. In addition, we would like to thank the University of Wisconsin Lidar Group for making
data from the M-PACE period available for evaluation via their website at <http://lidar.ssec.wisc.edu>, and the
M-PACE crew for their hard work in compiling the datasets used. Funding for M-PACE was provided by the
United States Department of Energy.

References

- 455 Barkstrom, B., Harrison, E., and Lee, R.: Earth Radiation Budget Experiment: Preliminary seasonal results, EOS, 71, 297, 1990.
- Clough, S., Shephard, M., Mlawer, E., Delamere, J., Iacono, M., Cady-Pereira, K., Boukabara, S., and Brown, P.: Atmospheric radiative transfer modeling: a summary of the AER codes, J. Quant. Spectrosc. Radiat. Transfer, 91, 233–244, 2005.
- 460 Curry, J. and Ebert, E.: Annual cycle of radiation fluxes over the Arctic Ocean: Sensitivity to cloud optical properties, J. Clim., 5, 1267–1280, 1992.
- Curry, J. and Herman, G.: Infrared radiative properties of summertime Arctic stratus clouds, J. Clim. Appl. Meteor., 24, 525–538, 1985.
- Curry, J., Rossow, W., Randall, D., and Schramm, J.: Overview of Arctic Cloud and Radiation Characteristics, 465 J. Climate, 9, 1731–1764, 1996.
- de Boer, G., Tripoli, G. J., and Eloranta, E. W.: Preliminary comparison of CloudSAT-derived microphysical quantities with ground-based measurements for mixed-phase cloud research in the Arctic, J. Geophys. Res., 113, D00A06, 10.1029/2008JD010029, 2008.
- de Boer, G., Eloranta, E., and Shupe, M.: Arctic Mixed-Phase Stratiform Cloud Properties from Multiple 470 Years of Surface-Based Measurements at Two High-Latitude Locations, J. Atmos. Sci., 66, 2874–2887, doi: 10.1175/2009JAS3029.1, 2009.
- de Boer, G., Hashino, T., and Tripoli, G. J.: A Theory for Ice Nucleation Through Immersion Freezing in Mixed-Phase Stratiform Clouds, Atmos. Res., 96, 315–324, doi: 10.1016/j.atmosres.2009.09.012, 2010.
- Dong, X. and Mace, G.: Arctic stratus cloud properties and radiative forcing derived from ground-based data 475 collected at Barrow, Alaska, J. Clim., 16, 445–461, 2003.
- Dong, X., Xi, B., Crosby, K., Long, C., Stone, R., and Shupe, M.: A 10 year climatology of Arctic cloud fraction and radiative forcing at Barrow, Alaska, J. Geophys. Res., 115, D17 212, 2010.
- Donovan, D. and van Lammeren, A.: Cloud effective particle size and water content profile retrievals using combined lidar and radar observations I – Theory and examples, J. Geophys. Res., 105, 27 425–27 488, 480 2001.
- Ebert, E. and Curry, J.: A parameterization of ice cloud optical properties for climate models, J. Geophys. Res., 97, 3831–3836, 1992.
- Eloranta, E.: High Spectral Resolution Lidar, in: Lidar: Range-Resolved Optical Remote Sensing of the Atmosphere, edited by Weitkamp, K., pp. 143–163, Springer-Verlag, 2005.
- 485 Intrieri, J., Fairall, C., Shupe, M., Persson, P., Andreas, E., Guest, P., and Moritz, R.: An annual cycle of Arctic surface cloud forcing at SHEBA, J. Geophys. Res., 107, 8039, 2002.
- IPCC: Climate Change 2007: The Physical Science Basis, Tech. rep., 2007.
- Kay, J. and Gettelman, A.: Cloud influence on and response to seasonal Arctic sea ice loss, J. Geophys. Res., 114, D18 204, doi:10.1029/2009JD011 773, 2009.
- 490 Long, C. and Shi, Y.: An automated quality assessment and control algorithm for surface radiation measurements, TOASJ, 2, 23–37, 2008.
- McFarquhar, G., Zhang, G., Poellot, M., Kok, G., McCoy, R., Tooman, T., Fridlind, A., and Heymsfield, A.: Ice Properties of Single-Layer Stratocumulus During the Mixed-Phase Arctic Cloud Experiment: 1.

- Observations, *J. Geophys. Res.*, 112, D24 201, 2007.
- 495 Mitchell, D.: Use of mass- and area-dimensional power laws for determining precipitation particle terminal velocities, *J. Atmos. Sci.*, 53, 1710–1723, 1996.
- Moran, K., Martner, B., Post, M., Kropfli, R., Welsch, D., and Widener, K.: An unattended cloud-profiling radar for use in climate research, *Bull. Am. Meteorol. Soc.*, 79, 443–455, 1998.
- Pinto, J.: Autumnal Mixed-Phase Cloudy Boundary Layers in the Arctic, *J. Atmos. Sci.*, 55, 2016–2038, 1998.
- 500 Prowse, T., Furgal, C., Wrona, F., and Reist, J.: Implications of climate change for northern Canada: freshwater, marine, and terrestrial ecosystems, *Ambio*, 38, 282–289, 2009.
- Ramanathan, V., Cess, R., Harrison, E., Minnis, P., Barkstrom, B., Ahmad, E., and Hartman, D.: Cloud-radiative forcing and climate: Results for the Earth Radiation Budget Experiment, *Science*, 243, 57–63, 1989.
- Schweiger, A. and Key, J.: Arctic Ocean radiative fluxes and cloud forcing estimates from the ISCPP C2 cloud dataset, 1983-1990, *J. Appl. Meteor.*, 33, 948–963, 1994.
- 505 Shupe, M. and Intrieri, J.: Cloud radiative forcing of the Arctic surface: The influence of cloud properties, surface albedo, and solar zenith angle, *J. Climate*, 17, 616–628, 2004.
- Shupe, M., Matrosov, S., and Uttal, T.: Arctic Mixed-Phase Cloud Properties Derived from Surface-Based Sensors at SHEBA, *J. Atmos. Sci.*, 63, 697–711, 2006.
- 510 Shupe, M., Daniel, J., de Boer, G., Eloranta, E., Kollias, P., Long, C., Luke, E., Turner, D., and Verlinde, J.: A Focus on Mixed-Phase Clouds: The Status of Ground-Based Observational Methods, *Bull. Am. Meteorol. Soc.*, 87, 1549–1562, 2008a.
- Shupe, M., Kollias, P., Poellot, M., and Eloranta, E.: On deriving vertical air motions from cloud radar Doppler spectra, *J. Atmos. Oceanic Technol.*, 25, 547–557, 2008b.
- 515 Stephens, G.: Remote sensing of the lower atmosphere, Oxford University Press, 1994.
- Uttal, T., Curry, J., McPhee, M., Perovich, D., Moritz, R., Maslanik, J., Guest, P., Stern, H., Moore, J., Turenne, R., Heiberg, A., Serreze, M., Wylie, D., and Persson, P.: Surface Heat Budget of the Arctic Ocean, *Bull. Am. Meteorol. Soc.*, 83, 255–275, 2002.
- Verlinde, J., Harrington, J., McFarquhar, G., Yannuzzi, V., Avramov, A., Greenberg, S., Johnson, N., Zhang, G., Poellot, M., Mather, J., Turner, D., Eloranta, E., Zak, B., Prenni, A., Daniel, J., Kok, G., Tobin, D., Holz, R., Sassen, K., Spangenberg, D., Minnis, P., Tooman, T., Ivey, M., Richardson, S., Bahrmann, C., Shupe, M., De Mott, P., Heymsfield, A., and Schofield, R.: The Mixed-Phase Arctic Cloud Experiment, *Bull. Am. Meteorol. Soc.*, 88, 205–221, 2007.
- 520 Westwater, E., Han, Y., Shupe, M., and Matrosov, S.: Analysis of integrated cloud liquid and precipitable water vapor retrievals from microwave radiometers during the Surface Heat Budget of the Arctic Ocean project, *J. Geophys. Res.*, 106, 32 019–23 030, 2001.
- Zuidema, P., Baker, B., Han, Y., Intrieri, J., Key, J., Lawson, P., Matrosov, S., Shupe, M., Stone, R., and Uttal, T.: An Arctic Springtime Mixed-Phase Boundary Layer Observed During SHEBA, *J. Atmos. Sci.*, 62, 160–176, 2005.

10 October 2004

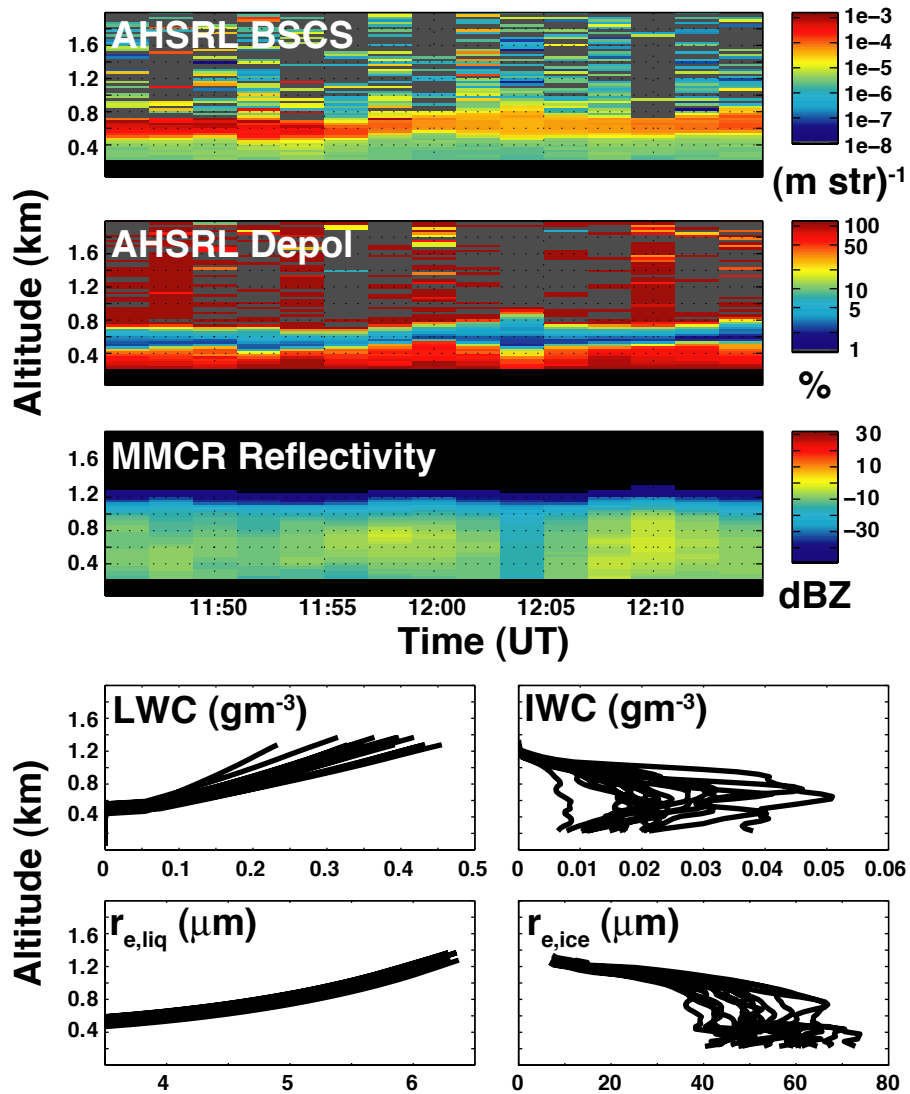


Fig. 1. Measured and retrieved cloud properties on 10 October, 2004. Included are (top to bottom) AHSRL backscatter cross-section, AHSRL depolarization ratio, MMCR reflectivity, and profiles of liquid water content (LWC), ice water content (IWC) and liquid ($r_{e,liq}$) and ice ($r_{e,ice}$) effective particle sizes.

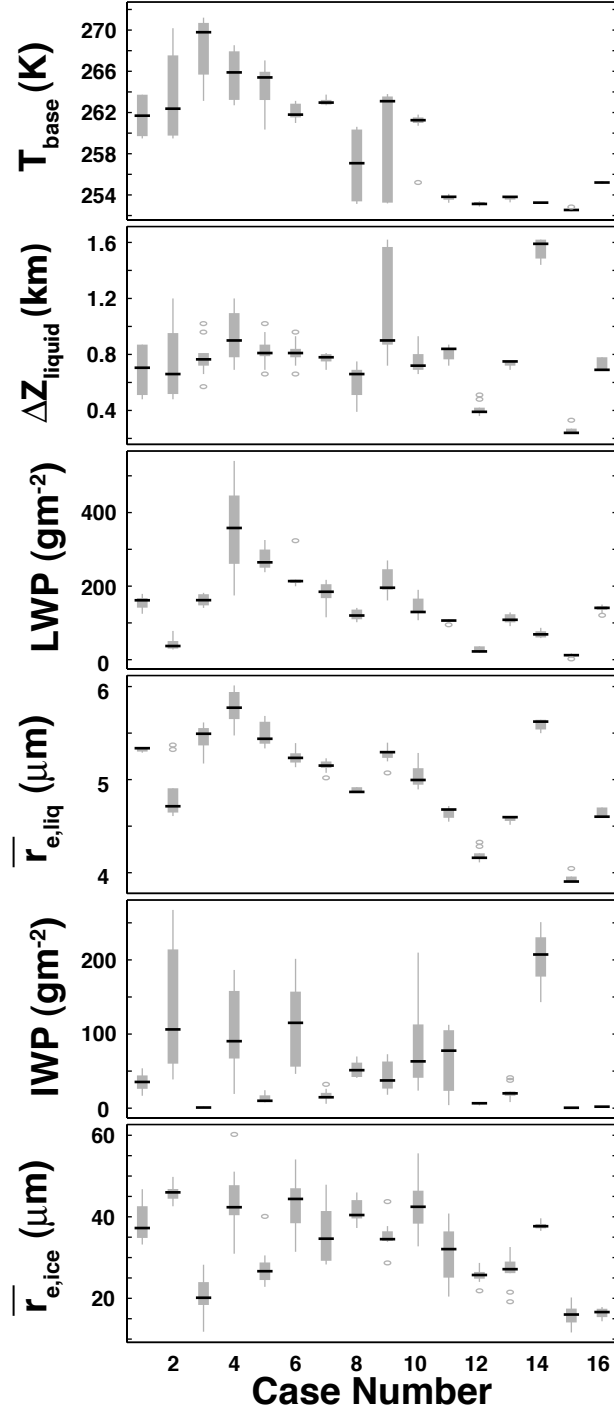


Fig. 2. Distributions of retrieved (top to bottom) cloud base temperature (T_{base}), liquid cloud thickness (ΔZ_{liquid}), liquid water path (LWP), mean liquid droplet effective radius ($\bar{r}_{e,liq}$), ice water path (IWP), and mean ice crystal effective radius ($\bar{r}_{e,ice}$) for all included cases

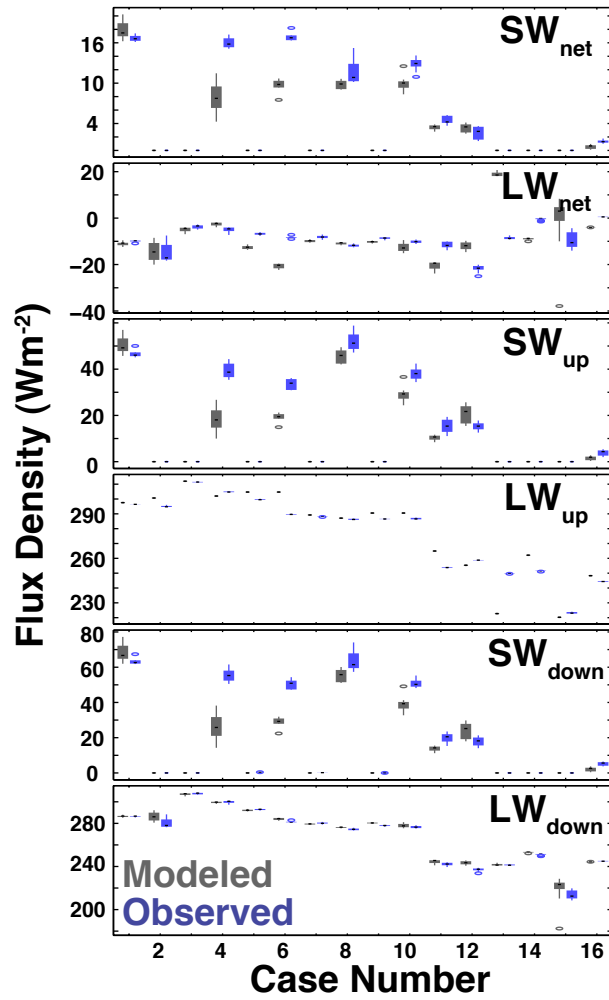


Fig. 3. Distributions of modeled (grey) and measured (blue) surface radiative flux densities. From top to bottom: net shortwave (SW_{net}), net longwave (LW_{net}), upward shortwave (SW_{up}), upward longwave (LW_{up}), downward shortwave (SW_{down}), and downward longwave (LW_{down}). The dots represent the case mean, the thick bar the 25th/75th percentiles, and the whiskers representing 1.5xIQR beyond 25th and 75th percentiles. Any values outside of that range are indicated by open circles.

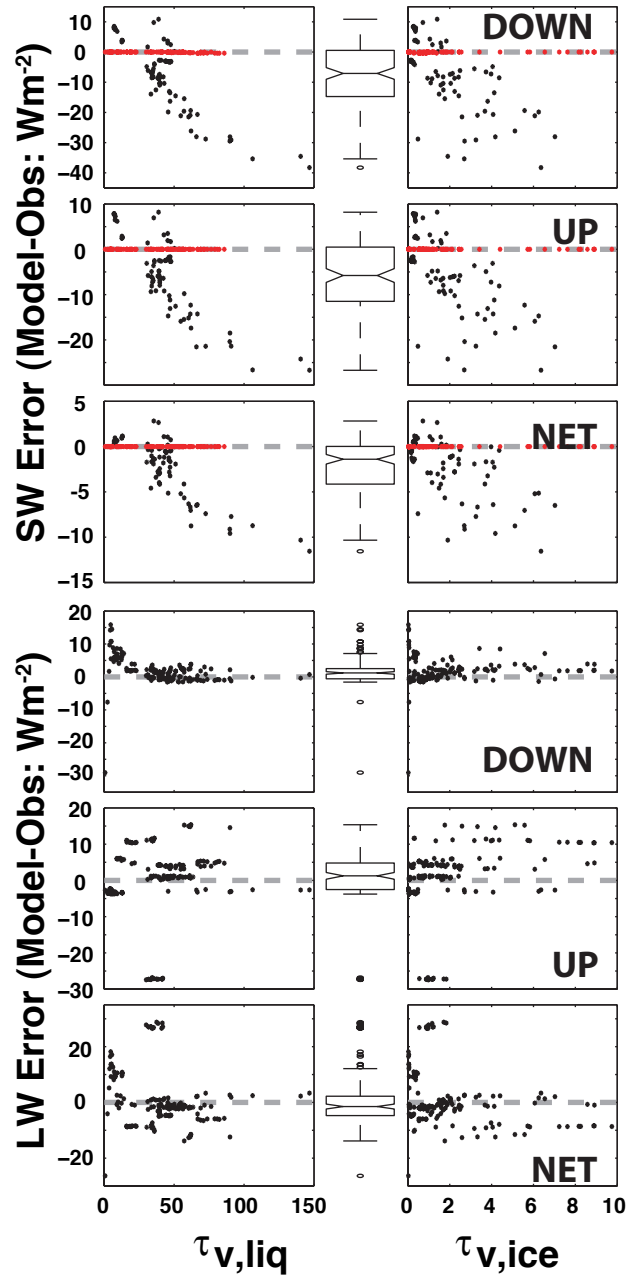


Fig. 4. Errors in modeled surface shortwave (SW, top three rows) and longwave (LW, bottom three rows) compared with liquid ($\tau_{v,liq}$, left) and ice ($\tau_{v,ice}$, right) visible optical thickness. Boxplots in between the liquid and ice comparisons provide error statistics, demonstrating the mean (center notch), IQR (ends of boxes), 1.5xIQR beyond 25th and 75th percentiles (ends of whiskers) and outliers (circles). For shortwave analysis, nighttime cases (red) are not included in the boxplots.

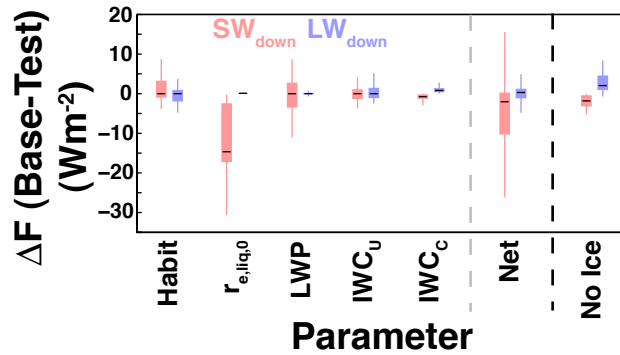


Fig. 5. Distributions of differences between downwelling shortwave (red) and longwave (blue) flux densities derived using base parameters (see text for details), and those derived with alternate values for the parameters shown. IWC_U represents the sensitivity of surface flux densities to IWC retrieval uncertainty, while IWC_C represents the sensitivity to the coefficient used in the empirical relationship. IWC_C is not accounted for in the net calculation shown. The no ice calculation on the far right compares clouds with ice included in radiative transfer calculations, and the same clouds with ice removed. The mean value is indicated by the black line in each distribution, the box indicates the IQR, and the whiskers represent $1.5 \times IQR$ beyond the 25th and 75th percentiles. Outliers are not shown, and nighttime cases are omitted in the shortwave evaluation.

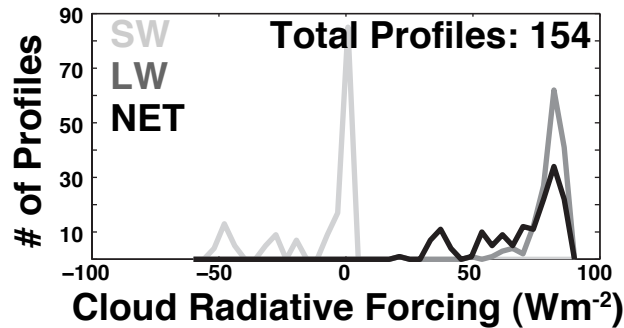


Fig. 6. Distributions of shortwave (SW, light grey), longwave (LW, dark grey) and net (black) cloud radiative forcing from M-PACE cases.

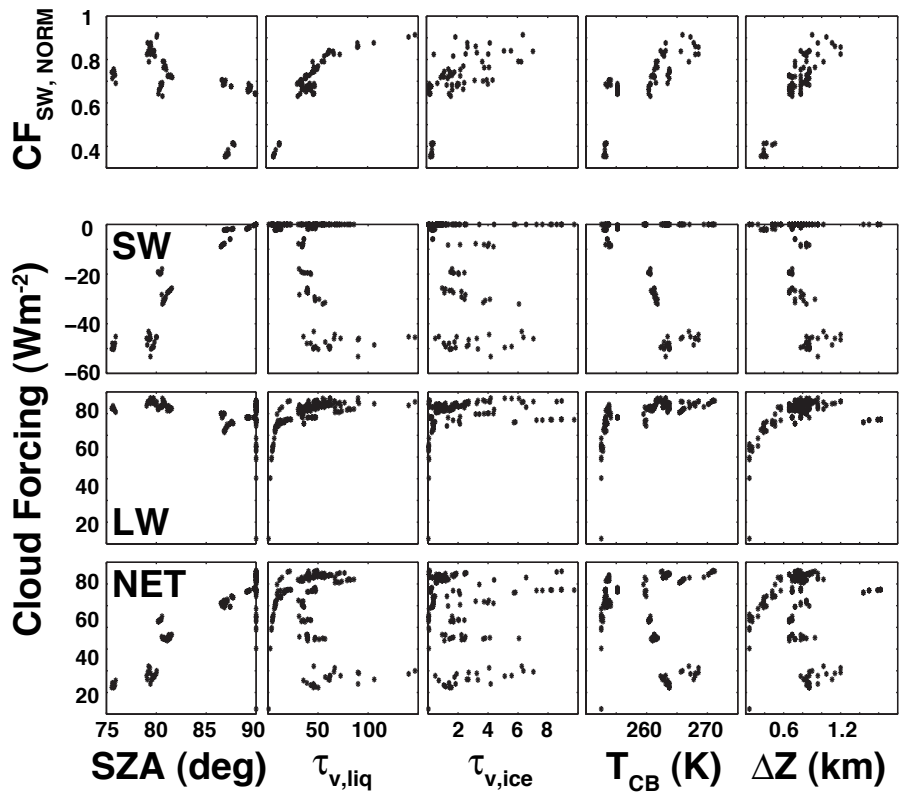


Fig. 7. Shortwave (SW, top), longwave (LW, middle) and net (bottom) cloud radiative forcing as a function of (from left to right) solar zenith angle (SZA), visible liquid optical depth ($\tau_{v,liq}$), visible ice optical depth ($\tau_{v,liq}$), cloud base temperature (T_{CB}), and cloud thickness (ΔZ) for profiles observed during M-PACE.

Table 1. Case overview providing case numbers, the time periods covered, and values for case mean liquid cloud depth, case mean liquid water path and case mean ice water path.

Case	Time Period	$\overline{\Delta Z}_{liq}$ (m)	\overline{LWP} (gm^{-2})	\overline{IWP} (gm^{-2})
01	2345 29 Sep - 0015 30 Sep	692	155.0	35.4
02	1145 01 Oct - 1215 01 Oct	754	43.1	132.7
03	1145 04 Oct - 1215 04 Oct	771	162.2	1.2
04	2345 08 Oct - 0015 09 Oct	934	352.4	108.7
05	1145 09 Oct - 1215 09 Oct	828	274.3	13.0
06	2345 09 Oct - 0015 10 Oct	812	229.4	115.2
07	1145 10 Oct - 1215 10 Oct	764	182.4	16.8
08	2345 11 Oct - 0015 12 Oct	619	121.8	52.4
09	1145 12 Oct - 1215 12 Oct	1144	210.3	42.9
10	2345 12 Oct - 0015 13 Oct	744	146.3	77.2
11	2345 29 Oct - 0015 30 Oct	803	106.0	62.1
12	2345 30 Oct - 0015 31 Oct	412	26.8	6.3
13	1145 02 Nov - 1215 02 Nov	734	110.6	21.6
14	1145 05 Nov - 1215 05 Nov	1547	70.4	202.2
15	1145 06 Nov - 1215 06 Nov	262	11.0	0.5
16	2345 07 Nov - 0015 08 Nov	726	138.4	2.0

Table 2. Mean errors in modeled surface radiative flux densities (model-observation). Total shortwave error estimates do not include nighttime cases

Case	$\overline{Error_{sw,dn}}$	$\overline{Error_{sw,up}}$	$\overline{Error_{sw,nt}}$	$\overline{Error_{lw,dn}}$	$\overline{Error_{lw,up}}$	$\overline{Error_{lw,nt}}$
	(Wm ⁻²)					
01	4.9	3.7	1.2	0.1	1.1	-1.0
02	0.0	0.0	0.0	5.8	5.6	0.2
03	0.0	0.0	0.0	-0.6	0.6	-1.2
04	-29.3	-21.2	-8.1	-0.4	-2.8	2.4
05	-0.4	0.0	0.0	-0.8	5.0	-5.8
06	-22.0	-14.6	-7.3	2.7	15.0	-12.4
07	-0.1	0.0	0.0	-0.4	0.9	-1.8
08	-8.4	-6.5	-1.9	1.7	0.8	0.9
09	0.0	0.0	0.0	2.5	4.0	-1.6
10	-12.1	-9.1	-3.0	1.2	3.8	-2.6
11	-6.0	-5.0	-1.1	2.3	11.2	-8.9
12	6.3	5.6	0.7	6.4	-3.4	9.8
13	0.0	0.0	0.0	0.2	-27.2	27.4
14	0.0	0.0	0.0	2.0	10.6	-8.6
15	0.0	0.0	0.0	5.0	-3.0	8.0
16	-3.1	-2.3	-0.7	-0.8	3.9	-4.7
M-PACE	-4.0	-2.8	-1.1	1.6	1.0	-0.7

Table 3. Mean cloud radiative forcing for M-PACE mixed-phase clouds by case, and for the entire period. The M-PACE mean shortwave cloud radiative forcing does not include nighttime cases.

Case	\overline{CRF}_{sw}	\overline{CRF}_{lw}	\overline{CRF}_{nt}
01	-48.6	82.1	33.5
02	0.0	79.9	79.9
03	0.0	85.1	85.1
04	-45.7	84.9	39.3
05	0.0	81.6	81.6
06	-49.8	86.1	36.4
07	0.0	83.6	83.6
08	-19.3	82.7	63.5
09	0.0	84.5	84.5
10	-28.5	83.7	55.2
11	-7.7	78.6	70.1
12	-2.0	74.1	72.1
13	0.0	82.3	82.3
14	0.0	76.9	76.9
15	0.0	58.8	58.8
16	-1.2	78.2	76.7
M-PACE	-25.3	80.2	67.5